Title

Control of Elemental Distribution in the Nanoscale Solid-State Reaction That Produces (Ga1—x Zn x)(N1—x O x) Nanocrystals

Journal

ACS Nano, 11(8)

ISSN

1936-0851

Authors

Tongying, Pornthip
Lu, Ying-Gang
Hall, Leah MG
et al.

Publication Date

2017-08-22

DOI

10.1021/acsnano.7b03891

Peer reviewed

ACSNANO
www.acsnano.org
ARTICLE

Control of Elemental Distribution in the Nanoscale Solid-State Reaction That Produces $(Ga_{1-x}Zn_x)(N_{1-x}O_x)$ Nanocrystals

Pornthip Tongying,[†] Ying-Gang Lu,[†,§] Leah M. G. Hall,[†] Kyureon Lee,[†,∥] Marta Sulima,[†] Jim Ciston,[‡] and Gordana Dukovic*[,†]

[†]Department of Chemistry and Biochemistry, University of Colorado Boulder, Boulder, Colorado 80309, United States
[‡]National Center for Electron Microscopy, Molecular Foundry, Lawrence Berkeley National Laboratory, Berkeley, California 94720, United States

Supporting Information

ABSTRACT: Solid-state chemical transformations at the nanoscale can be a powerful tool for achieving compositional complexity in nanomaterials. It is desirable to understand the mechanisms of such reactions and characterize the local-level composition of the resulting materials. Here, we examine how reaction temperature controls the elemental distribution in $(Ga_{1-x}Zn_x)(N_{1-x}O_x)$ nanocrystals (NCs) synthesized *via* the solid-state nitridation of a mixture of nanoscale ZnO and $ZnGa_2O_4$ NCs. $(Ga_{1-x}Zn_x)(N_{1-x}O_x)$ is a visible-light absorbing semiconductor that is of interest for applications in solar photochemistry. We couple elemental mapping using energy-dispersive X-ray spectroscopy in a scanning transmission electron microscope (STEM-EDS) with colocation analysis to study the elemental distribution and the degree of homogeneity in the $(Ga_{1-x}Zn_x)(N_{1-x}O_x)$ samples synthesized at temperatures ranging from 650 to 900 °C with varying ensemble compositions (*i.e.*, *x* values). Over this range of temperatures, the elemental distribution ranges from highly heterogeneous at 650 °C, consisting of a mixture of larger particles with Ga and N enrichment near the surface and very small NCs, to uniform particles with evenly distributed constituent elements for most compositions at 800 °C and above. We propose a mechanism for the formation of the $(Ga_{1-x}Zn_x)(N_{1-x}O_x)$ NCs in the solid state that involves phase transformation of cubic spinel $ZnGa_2O_4$ to wurtzite $(Ga_{1-x}Zn_x)(N_{1-x}O_x)$ and diffusion of the elements along with nitrogen incorporation. The temperature-dependence of nitrogen incorporation, bulk diffusion, and vacancy-assisted diffusion processes determines the elemental distribution at each synthesis temperature. Finally, we discuss how the visible band gap of $(Ga_{1-x}Zn_x)(N_{1-x}O_x)$ NCs varies with composition and elemental distribution.

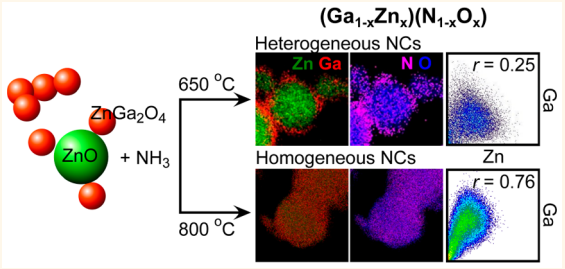

KEYWORDS: *nanocrystals, oxynitride, solid state, STEM-EDS, colocation, elemental correlation*

Emerging applications, such as solar fuel generation, have revealed the need for new semiconductors with binary and ternary compositions to control band gap and chemical stability.[1,2] While often desirable, compositional complexity can be difficult to achieve and requires synthetic control of composition at both the ensemble and local levels. For nanoscale semiconductors in particular, there has been remarkable development of solution phase chemical transformations that create ternary and quaternary mixed semiconductors.[3−5] Some materials, however, are not sufficiently reactive at temperatures compatible with solution phase reactions.[6] In these cases, chemical transformations in the solid state can provide an avenue for compositional complexity.[7−9] As nanoscale solid-state reactions emerge as means of achieving compositional complexity, it is necessary to understand their mechanisms and how the elemental distribution in the resulting materials can be controlled.

In this manuscript, we focus on the reaction that produces nanocrystals of the oxynitride $(Ga_{1-x}Zn_x)(N_{1-x}O_x)$. A solid solution of ZnO and GaN, $(Ga_{1-x}Zn_x)(N_{1-x}O_x)$ has gained considerable attention as a material for solar energy harvesting since 2005.[10] This material is unusual because it absorbs visible light even though its parent semiconductors, ZnO and GaN, have band gaps in the UV region (3.2 and 3.4 eV, respectively).[10−13] Decorated with suitable cocatalysts, $(Ga_{1-x}Zn_x)(N_{1-x}O_x)$ is capable of splitting water into H_2 and O_2 under visible light illumination (λ >400 nm).[10−22]

Received: June 2, 2017
Accepted: July 31, 2017
Published: July 31, 2017

DOI: 10.1021/acsnano.7b03891
ACS Nano 2017, 11, 8401−8412

In $(Ga_{1-x}Zn_x)(N_{1-x}O_x)$, the composition (*i.e.*, the value of x) determines the band gap, which in turn determines the fraction of the solar spectrum that can be absorbed.[13,23,24] Although composition control has been made difficult by Zn volatility at high temperatures, several synthesis methods have been developed to widen the range of available compositions of $(Ga_{1-x}Zn_x)(N_{1-x}O_x)$.[10,23−29] One of these methods is a solid-state synthesis of $(Ga_{1-x}Zn_x)(N_{1-x}O_x)$ *nanocrystals* in which a mixture of ZnO (~10 nm) and $ZnGa_2O_4$ (~5 nm) NCs is converted to $(Ga_{1-x}Zn_x)(N_{1-x}O_x)$ under NH_3 at 650 °C.[23] The use of nanoscale precursors allows for a lower conversion temperature and avoids the loss of Zn. As a consequence, a wide range of compositions is possible ($0.06 \leq x \leq 0.98$) simply by tuning the starting material ratio, although, as $ZnGa_2O_4$ has the x value of 0.33, Ga-rich compositions require a slight increase in temperature to remove Zn.[24] The wide range of compositions results in band gaps that vary from 2.9 to 2.2 eV.[24]

While the x values reported above describe the average ensemble composition of nanocrystalline $(Ga_{1-x}Zn_x)(N_{1-x}O_x)$ samples, the question of how the four elements are distributed within and among particles has not been answered. Because ZnO, GaN, and $(Ga_{1-x}Zn_x)(N_{1-x}O_x)$ have similar lattice parameters, the *crystalline* order may coexist with varying degrees of *compositional* disorder.[30,31] The solid-state reaction that transforms ZnO and $ZnGa_2O_4$ NCs into $(Ga_{1-x}Zn_x)(N_{1-x}O_x)$ under NH_3 flow is a complex process, requiring both the making and breaking of chemical bonds and diffusion of elements to create the final product. Thus, it is important to understand how the interplay of these factors leads to the elemental distribution in the final product.

In this manuscript, we reveal the elemental distribution in $(Ga_{1-x}Zn_x)(N_{1-x}O_x)$ NCs synthesized over a range of temperatures from 650 to 900 °C using subnanometer EDS mapping in STEM. The elemental composition of the NCs at the ensemble and the individual particle levels is measured by inductively coupled plasma optical emission spectroscopy (ICP-OES) and STEM-EDS quantification, respectively. We use colocation analysis of EDS maps to quantify the degree of correlation in elemental distribution by determining the Pearson product-moment correlation coefficient (PCC or Pearson's r) for Ga and Zn. We find a considerable degree of heterogeneity in samples of $(Ga_{1-x}Zn_x)(N_{1-x}O_x)$ NCs synthesized at 650 °C, consisting of two distinct types of particles and compositional heterogeneity within particles. The elemental distribution is readily controllable with reaction temperature, which increases homogeneity and reaches an even distribution of the four elements at 800 °C. We explain these results in terms of increased chemical reactivity, faster diffusion, and vacancy-assisted diffusion at higher temperatures. Finally, we discuss the relationships between the compositional distribution and the optical properties of the $(Ga_{1-x}Zn_x)(N_{1-x}O_x)$ samples.

RESULTS

We begin our investigation of elemental distribution with the samples of $(Ga_{1-x}Zn_x)(N_{1-x}O_x)$ NCs synthesized at 650 °C, the temperature at which the loss of Zn is minimal.[23,24] By nitriding a starting mixture of wurtzite ZnO (d ~10 nm) and cubic spinel $ZnGa_2O_4$ (d ~5 nm) NCs at this temperature, compositions ranging from $x = 0.38$ to $x = 0.98$ can be obtained simply by varying the ratio of the starting material NCs to match the Zn:Ga ratio desired in the final product.[23,24] These x values refer to the ensemble composition of the product measured by elemental analysis of acid-digested samples using ICP-OES. Powder X-ray diffraction (XRD) and TEM imaging have shown that the products contain single crystalline wurtzite particles with diameters of 15−20 nm, such as the one shown in Figure 1. Their XRD peak positions fall between those of

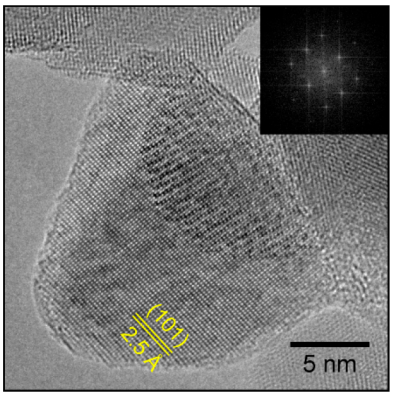

Figure 1. High-resolution TEM image of a single-crystalline $(Ga_{1-x}Zn_x)(N_{1-x}O_x)$ particle ($x = 0.76$), with fast Fourier transform (inset).

wurtzite ZnO and GaN, consistent with the formation of a solid solution, with an upward bowing deviation from Vegard's law in lattice constants.[23,24] For this study, we selected the ensemble x values of 0.38, 0.52, 0.75, and 0.93 to span the composition range achieved at 650 °C. Their XRD patterns are shown in Figure S1.

Heterogeneous Elemental Distribution in $(Ga_{1-x}Zn_x)(N_{1-x}O_x)$ Particles Synthesized at 650 °C. We first examine the elemental distribution in individual $(Ga_{1-x}Zn_x)(N_{1-x}O_x)$ particles made at 650 °C. Figure 2 shows high-angle annular dark-field (HAADF)-STEM image and EDS elemental maps of Zn, Ga, O, and N, and line profiles of Zn and Ga taken on a $(Ga_{1-x}Zn_x)(N_{1-x}O_x)$ particle in a sample with the ensemble composition of $x = 0.38$. The elemental maps clearly

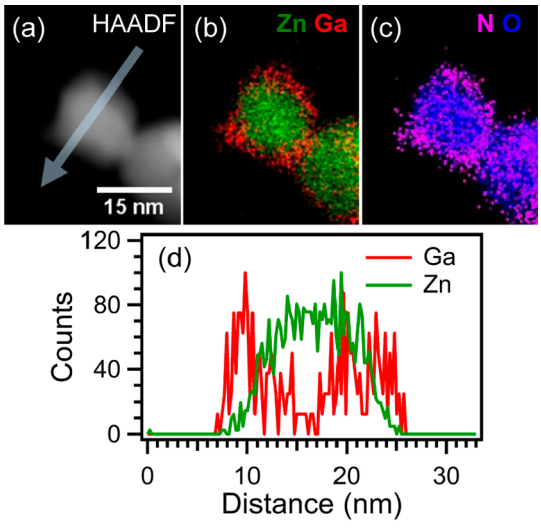

Figure 2. (a) HAADF-STEM image and (b,c) the corresponding EDS elemental maps of $(Ga_{1-x}Zn_x)(N_{1-x}O_x)$ NCs with ensemble $x = 0.38$ synthesized at 650 °C. (d) EDS line profiles taken across the oxynitride particle indicated in (a) with an arrow.

DOI: 10.1021/acsnano.7b03891
ACS Nano 2017, 11, 8401−8412

demonstrate that the four elements are not distributed homogeneously (Figure 2b,c). Zn and O are more heavily concentrated at the particle core while Ga and N are preferentially found closer to the particle surface. EDS line profiles taken across one particle further illustrate the nonuniform distribution of Zn and Ga (Figure 2d). EDS maps of the individual elements and additional overlap maps can be found in Figure S2. We observe similar behavior throughout the sample, with strong spatial correlation between Ga and N, as well as Zn and O, and the enrichment of the former around edges and the latter in the particle center. The EDS elemental maps of the large particles with other ensemble compositions (x = 0.52, 0.75 and 0.93) are shown in Figure 3

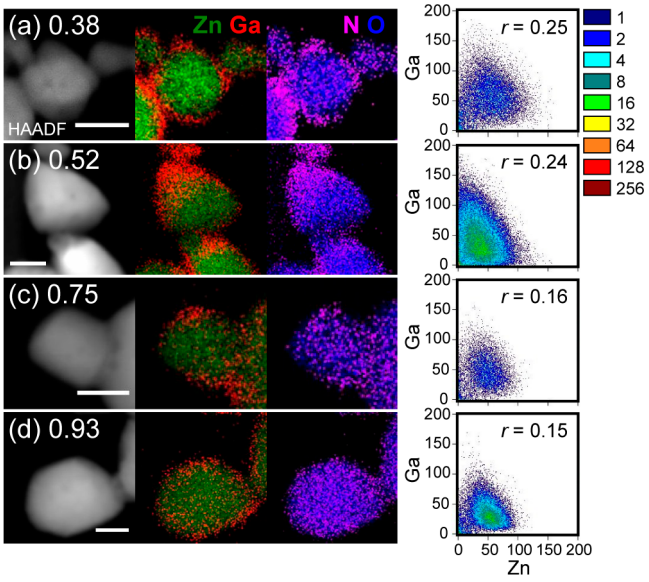

Figure 3. Left column: HAADF-STEM images and EDS elemental maps of $(Ga_{1-x}Zn_x)(N_{1-x}O_x)$ NCs synthesized at 650 °C with varying ensemble compositions x of (a) 0.38, (b) 0.52, (c) 0.75 and (d) 0.93. The map shows the overlays of two elements, Zn/Ga and N/O. Scale bars are 15 nm. Right column: Colocation analyses of the distribution of Zn in relation to Ga for each $(Ga_{1-x}Zn_x)(N_{1-x}O_x)$ NC shown on the left. Analyses contain scatter plots of the respective element intensities at each pixel within the single NC area. The resulting Pearson's r value is displayed in the top right corner of the scatter plot.

(and Figure S3). These particles show a remarkably similar pattern of compositional heterogeneity, with Zn and O enrichment inside the particles and Ga and N enrichment near the surface.

To describe the degree of compositional heterogeneity in samples shown in Figures 2 and 3, we turn to colocation analysis, which quantifies the spatial correlation of elements within a particle. We use methods similar to those previously reported for a Mn−Co bimetallic catalyst[32] and nickel distribution in cell-mineral aggregates formed by Fe(II)-oxidizing bacteria.[33] The scatter plots for Zn and Ga intensities at each pixel within the area of one particle are shown in Figure 3 (right column). The scatter plot and colocation analysis section in Materials and Methods describes how the plots are generated. The intensities of Zn and Ga are in units of atomic percent obtained from the quantification of four elements (Zn, Ga, N and O). As shown in the right column of Figure 3, we observe some preference for higher Ga content when Zn is low, resulting in somewhat triangular shape of the correlation plots. A plot that deviates from a linear relationship and has a fairly spread out shape reflects a weak correlation.[34] The correlation can be quantified by Pearson's r,[35] which characterizes the correlation between two variables, in our case, the intensities of Zn and Ga and is calculated using eq 1 (in Materials and Methods). Pearson's r can range from −1 to 1, where 1 represents perfect positive correlation, 0 indicates no correlation and −1 indicates perfect negative correlation. For interpretation, Pearson's r values are categorized as weak (<0.35), moderate (0.36−0.67) and high (0.68−1) correlations.[34] The resulting Pearson's r values obtained from the scatter plots of 650 °C samples are in the range of 0.15−0.25, suggesting a weak correlation of Zn and Ga, which is consistent with the visual inspection of the elemental maps. The origin of this heterogeneity will be described in the Discussion section. We note that we do not observe evidence for phase separation of pure GaN and ZnO in the scatter plots. Likewise, XRD patterns of these $(Ga_{1-x}Zn_x)(N_{1-x}O_x)$ samples cannot be described with a sum of GaN and ZnO peaks (Figure S1).

Impact of Synthesis Temperature on the Elemental Distribution in $(Ga_{1-x}Zn_x)(N_{1-x}O_x)$ NCs. Because the synthesis of $(Ga_{1-x}Zn_x)(N_{1-x}O_x)$ NCs is a solid-state chemical transformation, it is reasonable to expect that its trajectory will have a strong dependence on reaction temperature. We therefore examine how the reaction temperature impacts the elemental distribution in $(Ga_{1-x}Zn_x)(N_{1-x}O_x)$ NCs. A mixture of starting materials, ZnO and $ZnGa_2O_4$ NCs having the same molar ratio (Zn/Ga ~10, x ~0.91) was heated under NH_3 at different reaction temperatures: 650, 750, 800, 850, and 900 °C. After a 10 h reaction time, we obtained $(Ga_{1-x}Zn_x)(N_{1-x}O_x)$ samples with different ensemble x values, as determined by ICP-OES analysis: 0.93, 0.27, 0.11, 0.11 and 0.08, respectively. Zn evaporation at high temperatures (≥750 °C) in an NH_3 atmosphere[10,13,23,36] causes a significant decrease in ensemble x values in the product compared to the starting material mixture (x ~0.91).

Figure 4 (and Figure S4) shows HAADF images and STEM-EDS elemental maps of the $(Ga_{1-x}Zn_x)(N_{1-x}O_x)$ NCs prepared at different nitridation temperatures. EDS elemental maps paired with line scan profiles taken across individual particles show that the distribution of elements becomes more uniform with increasing nitridation temperature. At 750 °C, there is still some separation of Ga and Zn (Figure 4b) and N and O (Figure S4b). As in the 650 °C samples, the Ga position correlates with N, and Zn correlates with O. Particles synthesized at 800, 850, and 900 °C appear to have all elements distributed evenly throughout.

Because of Zn evaporation, increasing the nitridation temperature affects both the elemental distribution and the composition. To separate the two effects, we synthesized samples of similar compositions at 650, 700, 750, and 800 °C. To do this, we adjusted the starting material composition (*i.e.*, the ratio of ZnO to $ZnGa_2O_4$) to obtain $(Ga_{1-x}Zn_x)(N_{1-x}O_x)$ samples with similar final ensemble x values of ~0.35. Ratios of Zn/Ga in the starting materials were adjusted to ~0.64, 1, 2, and 20 for the nitridation at 650, 700, 750, and 800 °C, respectively, with a nitridation time of 10 h for the first three reaction temperatures and 4 h for 800 °C. TEM images of the resulting particles are shown in Figure S5. The particle sizes increase with increasing nitridation temperatures: 17.3 ± 3.7, 18.9 ± 4.1, 18.4 ± 6.0 and 40.2 ± 10.5 nm, respectively. A similar observation has been made previously.[37] XRD patterns

DOI: 10.1021/acsnano.7b03891
ACS Nano 2017, 11, 8401−8412

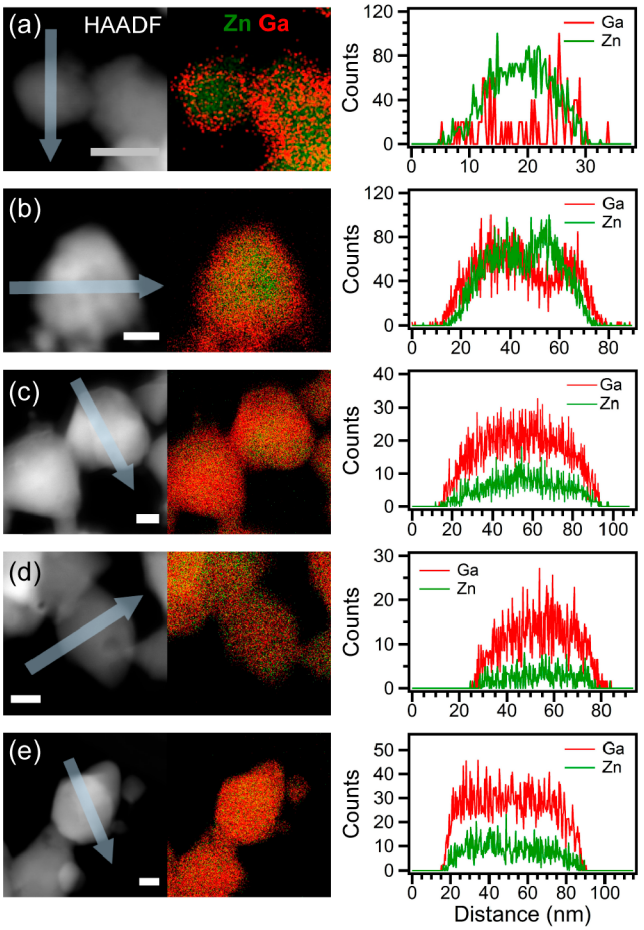

Figure 4. HAADF-STEM images and EDS elemental maps of $(Ga_{1-x}Zn_x)(N_{1-x}O_x)$ NCs obtained from the same Zn/Ga ratio in the starting materials at varying reaction temperatures: (a) 650 (x = 0.93), (b) 750 (x = 0.27), (c) 800 (x = 0.11), (d) 850 (x = 0.11) and (e) 900 (x = 0.08) °C. Scale bars are 20 nm. EDS line profiles of Zn and Ga (right column) taken across an oxynitride particle are marked by an arrow for the direction of the profile.

of these samples are shown in Figure S6. All samples show a wurtzite crystal structure with diffraction peaks located between the wurtzite peaks of the parent materials, ZnO and GaN. The crystallite sizes obtained from XRD data are estimated using the Scherrer equation (Table S1). They are in good agreement with particle sizes determined by low-magnification TEM (Figure S5), indicating that the particles are single crystals.

Representative HAADF images and STEM-EDS elemental maps of the $(Ga_{1-x}Zn_x)(N_{1-x}O_x)$ NCs with similar ensemble x values prepared at different nitridation temperatures (650, 700, 750, and 800 °C) are shown in Figure 5. The EDS elemental maps show that the homogeneity in the samples increases with increasing nitridation temperature while the ensemble composition remains the same. The scatter plots of the intensities of Zn and Ga for the particle area are shown in the right column. The degree of homogeneity is quantified by the Pearson's r, the value of which is shown on the right corner of each scatter plot. A weak correlation of Zn and Ga is found in the samples synthesized at 650 and 700 °C (r = 0.17 and 0.13, respectively). At 750 °C, the Pearson's r is 0.45, which is considered as moderate correlation, while the NCs synthesized at 800 °C have a strong correlation (r = 0.76).

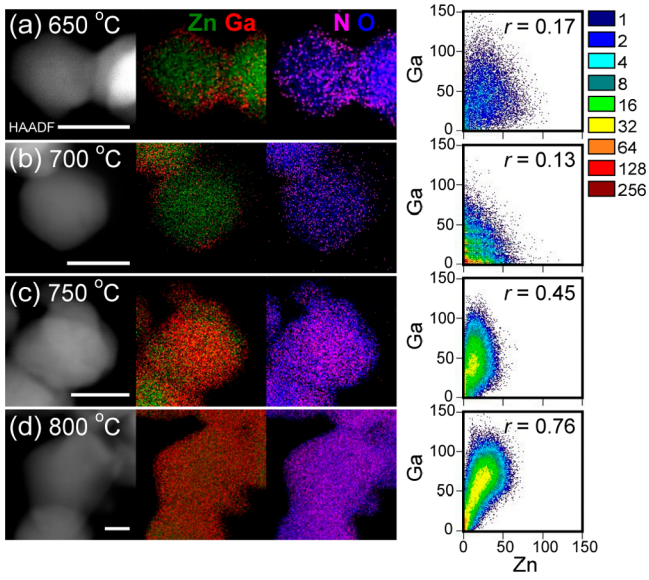

Figure 5. HAADF images and EDS elemental maps of $(Ga_{1-x}Zn_x)(N_{1-x}O_x)$ NCs with similar ensemble x values of ~0.35 synthesized at (a) 650, (b) 700, (c) 750 and (d) 800 °C. Scale bars are 20 nm. Right column: the scatter plots of the intensity of Zn and Ga with the value of Pearson's r in the upper right corner.

Composition-Dependent Elemental Distribution of $(Ga_{1-x}Zn_x)(N_{1-x}O_x)$ NCs Synthesized at 800 °C. On the basis of the temperature dependence of the products of the $(Ga_{1-x}Zn_x)(N_{1-x}O_x)$ synthesis, we conclude that by 800 °C, the products have a homogeneous elemental distribution within each particle, at least within the limits of the resolution of the EDS mapping. To some extent, we can compensate for the Zn evaporation at the higher reaction temperature (800 *vs* 650 °C) by shortening the reaction time (<10 h). In this section, we examine the relationships between synthesis conditions, composition, and elemental distribution. The syntheses of $(Ga_{1-x}Zn_x)(N_{1-x}O_x)$ NCs using a mixture of ZnO and $ZnGa_2O_4$ NCs with Zn/Ga ratio of 20:1 are carried out at 800 °C for 10, 6, 4, 3, and 2 h. The resulting $(Ga_{1-x}Zn_x)(N_{1-x}O_x)$ NCs have ensemble x values of 0.11, 0.21, 0.35, 0.44 and 0.86, respectively, as determined by ICP-OES.

Representative HAADF images and STEM-EDS elemental maps of the $(Ga_{1-x}Zn_x)(N_{1-x}O_x)$ NCs with ensemble x values of 0.11, 0.21, 0.35, and 0.44 are shown in Figure 6 (and Figure S7) (the sample with x = 0.86 will be discussed later). EDS elemental maps of the particle and line profiles of Zn and Ga taken across a single particle clearly show that the individual elements are homogeneously distributed in the particles. Under our conditions, 3 h is the shortest reaction time that is sufficiently long to yield homogeneous NCs with an ensemble x value as high as 0.44. The NCs synthesized at 800 °C for 2 h do not reach homogeneity, as we will discuss below. A single area EDS analysis shown in Figure S8 reveals that there is minimal difference in the composition near the particle surface (Ga ~30.6 at.% and Zn ~22.0 at.%) and the particle core (Ga ~31.6 at.% and Zn ~19.7 at.%). To quantify the degree of elemental correlation of the samples with different compositions, scatter plot and PCC statistical analysis are carried out, as shown in the right column in Figure 6. A qualitative examination of scatter plots of four samples shows that the relationship between Zn and Ga approaches a linear shape. The Pearson's r of the four compositions is in the range of 0.74–0.80, indicating strong

DOI: 10.1021/acsnano.7b03891
ACS Nano 2017, 11, 8401–8412

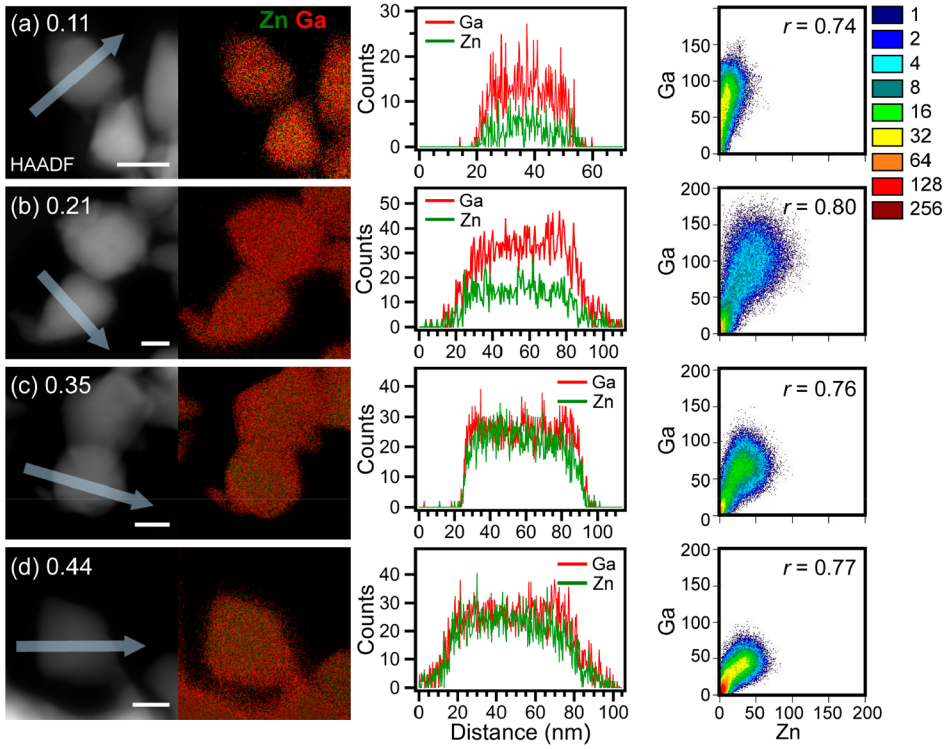

Figure 6. Left column: HAADF-STEM images and EDS elemental maps of $(Ga_{1-x}Zn_x)(N_{1-x}O_x)$ NCs prepared at 800 °C with ensemble x values of (a) 0.11, (b) 0.21, (c) 0.35 and (d) 0.44. Scale bars are 30 nm. Middle column: EDS line profiles of Zn and Ga taken across an oxynitride particle indicated by arrow for the direction of the profile. Right column: Colocation analyses of the distribution of Zn in relation to Ga for $(Ga_{1-x}Zn_x)(N_{1-x}O_x)$ NCs. Analyses contain scatter plots of the respective element intensities at each pixel within the single NC area. The resulting Pearson's r is displayed in the top right corner of the scatter plot.

correlation between Zn and Ga. The slope of the line is approximately the ratio of Ga to Zn.

While the reaction temperature is a key factor in elemental distribution, the reaction time also plays an important role. The $(Ga_{1-x}Zn_x)(N_{1-x}O_x)$ NCs synthesized at 800 °C for 2 h have an ensemble x value of 0.86. Representative HAADF-STEM image, STEM-EDS elemental maps and line scan profiles of Zn and Ga are illustrated in Figure S9. These images show NCs with heterogeneous elemental distribution similar to samples made at 650 °C. It appears that at 2 h, the reaction time is not long enough to achieve strong elemental correlation.

To enable comparisons with $(Ga_{1-x}Zn_x)(N_{1-x}O_x)$ NC samples synthesized at 650 °C, which have been previously characterized with XRD and TEM imaging,[23,24] we describe the results of similar characterization of the $(Ga_{1-x}Zn_x)(N_{1-x}O_x)$ NCs synthesized at 800 °C. Low-magnification TEM images of the $(Ga_{1-x}Zn_x)(N_{1-x}O_x)$ NCs with ensemble x values of 0.11, 0.21, 0.35, and 0.44 are shown in Figure S10. The NCs have an average particle dimension of ~35−41 nm as measured by TEM, which is in good agreement with the crystallite size obtained from XRD using the Scherrer equation, shown in Table S2, indicating that the particles are single crystals. The positions of the diffraction peaks shown in Figure S11a are located between those of GaN and ZnO, consistent with a solid solution of GaN and ZnO. The diffraction peaks are shifted to lower angles (toward ZnO peaks) with increasing ensemble x value. The lattice parameters, a and c, of the 800 °C products plotted against ensemble x values are shown in Figure S11b. They deviate from the parameters of an ideal solid solution of the parent compounds, ZnO and GaN, with upward bowing, as has been theoretically predicted[31,38] and observed in $(Ga_{1-x}Zn_x)(N_{1-x}O_x)$ synthesized by other methods.[26,39]

The optical properties of the $(Ga_{1-x}Zn_x)(N_{1-x}O_x)$ NCs prepared at 800 °C were measured by diffuse reflectance spectroscopy. Using the Kubelka−Munk equation, the diffuse reflectance spectra were transformed to absorption spectra, which are presented in Figure 7. The absorption edges of the NCs are shifted to longer wavelengths with increasing values of x. As with other $(Ga_{1-x}Zn_x)(N_{1-x}O_x)$ materials, the absorption onsets in these samples are lower in energy than the band gaps of ZnO (3.2 eV) and GaN (3.4 eV). This dependence of visible band gap on composition is a signature feature of $(Ga_{1-x}Zn_x)$-$(N_{1-x}O_x)$ materials and the results in Figure 7 are consistent

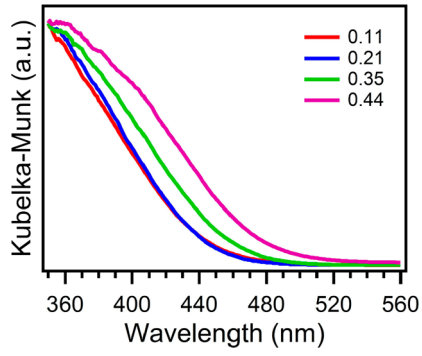

Figure 7. Kubelka−Munk transformed diffuse reflectance spectra of $(Ga_{1-x}Zn_x)(N_{1-x}O_x)$ NCs synthesized at 800 °C with different compositions (x = 0.11, 0.21, 0.35 and 0.44). The spectra are normalized at 350 nm.

DOI: 10.1021/acsnano.7b03891
ACS Nano 2017, 11, 8401−8412

with previous observations.[13,26] The optical properties of these samples will be addressed in the Discussion section.

Presence of Additional Species in $(Ga_{1-x}Zn_x)(N_{1-x}O_x)$ Samples Synthesized at 650 °C. Quantitative EDS analysis of local composition in $(Ga_{1-x}Zn_x)(N_{1-x}O_x)$ samples prepared at 650 °C reveals a stark discrepancy between the ensemble x values and those of individual particles. For example, quantitative analysis of the composition in the core and surface areas of the particle in Figure 2 shows that the x values in the two regions are 0.97 and 0.50, respectively (Figure S12). The x value for the entire particle is 0.83, which is considerably higher than the ensemble x value for the sample of 0.38 measured by ICP-OES. Similarly, the single area quantitative EDS compositional analysis on a particle of the $(Ga_{1-x}Zn_x)(N_{1-x}O_x)$ sample having high ensemble x value (x = 0.76) shows that two regions (tip and core) have x values of 0.30 and 0.97, respectively, with the overall particle x value of 0.86 (Figure S13). A quantitative analysis of 96 individual particles from samples with the four different ensemble x values (Figure S14) shows a remarkable result: the individual large wurtzite particles have x values of 0.8−0.9, even though the ensemble x values range from 0.38 to 0.93 (Table 1).

Table 1. Elemental Composition, x, in Ensemble and Individual $(Ga_{1-x}Zn_x)(N_{1-x}O_x)$ NCs Synthesized at 650 °C Examined by ICP-OES and EDS Elemental Analyses, Respectively

composition, x	
ICP-OES (ensemble)	EDS quantification (single particle)
0.38	0.85 ± 0.04
0.52	0.86 ± 0.04
0.75	0.92 ± 0.02
0.93	0.95 ± 0.02

The discrepancy in x values between individual $(Ga_{1-x}Zn_x)(N_{1-x}O_x)$ particles and the ensemble sample suggests that not all of the Ga and N are contained in the wurtzite nanocrystals shown in Figures 2 and 3. A careful examination of low-magnification TEM images of $(Ga_{1-x}Zn_x)(N_{1-x}O_x)$ samples prepared at 650 °C reveals the presence of an additional type of structure: much smaller (5.4 ± 1.3 nm), aggregated particles. Figure 8a shows the presence of such particles in the x = 0.38 sample alongside the large particles discussed above. The small particle aggregates are more common at lower ensemble x values (see, for example, Figure S15).

We suspected that these small aggregated particles might arise from nitridation of the $ZnGa_2O_4$ nanocrystals that are not adjacent to ZnO particles during the reaction. We have previously proposed that the $(Ga_{1-x}Zn_x)(N_{1-x}O_x)$ NCs such as the ones shown in Figures 2 and 3 arise from a mechanism in which $(Ga_{1-x}Zn_x)(N_{1-x}O_x)$ nucleates at the interface of a ZnO and a $ZnGa_2O_4$ nanocrystal,[24] with ZnO providing a crystalline template for topotactic growth of $(Ga_{1-x}Zn_x)(N_{1-x}O_x)$. If the $ZnGa_2O_4$ nanocrystal is not in sufficient proximity to a ZnO nanocrystal, it may still produce a nitrided product, but one with a different morphology and crystal structure. To test this hypothesis, we carried out nitridation of $ZnGa_2O_4$ at 650 °C in the absence of ZnO. The resulting material consists of small aggregated particles of similar appearance (Figure 8b) (a low-magnification TEM image is shown in Figure S16). The XRD pattern shows one very broad peak with the base covering 30−40° (see Figure 8c). Because of the broad XRD peaks caused by the small particle size, it is difficult to unambiguously determine whether the crystal structure of this product is spinel, wurtzite, or a mix of the two. Spinel zinc gallium oxynitrides have been previously observed to coexist with wurtzite oxynitride under certain synthesis conditions.[40,41] Nitrided $ZnGa_2O_4$ shows a clear wurtzite pattern at reaction temperatures of 750 °C and above.[24] STEM-EDS mapping of the $ZnGa_2O_4$ particles nitrided at 650 °C (see Figure 8d) shows uniform distribution of Zn, Ga, N, and O. Quantification results of seven areas (~50 × 50 nm) give x value of 0.14 ± 0.01 which is in agreement with 0.13 ± 0.00 obtained from ICP-OES. Figure S17 shows the Kubelka−Munk absorption spectrum of these small particles. Its absorption edge is in the visible region with the absorption onset ~475 nm. On the basis of the XRD, optical, and elemental mapping data, these small particles appear to also be $(Ga_{1-x}Zn_x)(N_{1-x}O_x)$, only with ambiguous crystal structure and smaller particle size. For the purposes of this manuscript,

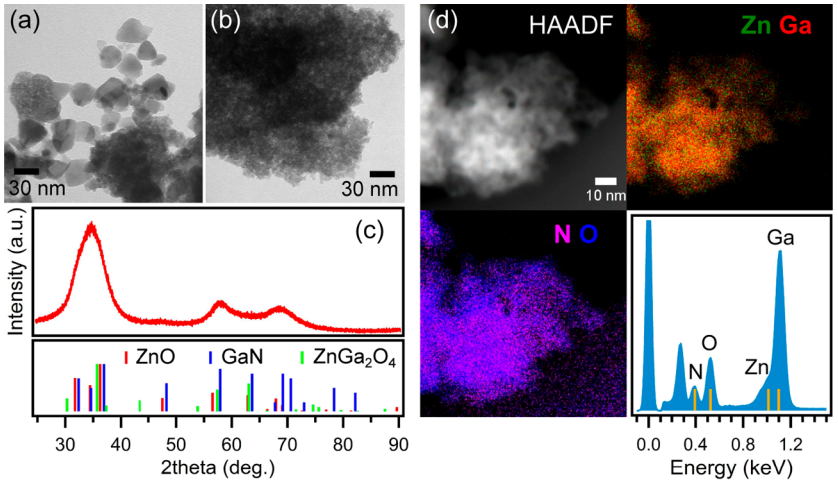

Figure 8. Low-magnification TEM images of (a) $(Ga_{1-x}Zn_x)(N_{1-x}O_x)$ NCs with x = 0.38 and (b) nitrided $ZnGa_2O_4$ at 650 °C. (c) Powder XRD pattern of nitrided $ZnGa_2O_4$. The vertical lines represent the reference diffraction patterns of $ZnGa_2O_4$ (green, JCPDS #38−1240), ZnO (red, JCPDS #05−0664), and GaN (blue, JCPDS #2−1078). (d) HAADF image and EDS elemental maps and spectrum of the nitrided $ZnGa_2O_4$.

DOI: 10.1021/acsnano.7b03891
ACS Nano 2017, 11, 8401−8412

we will refer to this product as "nitrided $ZnGa_2O_4$". We note that the nitrided $ZnGa_2O_4$ samples tend to have lower Zn content than expected from starting material. This may be due to increased Zn evaporation when ZnO is not available nearby. The x value of this particular sample was particularly low. Normally, they are in the 0.25−0.30 range.

We now turn back to the composition of the samples with varying ensemble x values synthesized at 650 °C. It appears that these samples are a mixture of the small aggregated particles, such as the ones described above, and the large wurtzite particles with heterogeneous composition shown in Figures 2 and 3. Further evidence for this is present in the XRD patterns. For example, for the x = 0.38 sample, a contribution of the broad peak arising from nitrided $ZnGa_2O_4$ can be seen underneath the dominant wurtzite peaks associated with the large particles (Figure S18). The varying ensemble x values can then arise from a different ratio of the two types of particles. Starting material mixtures for the higher x values have proportionally more ZnO NCs, allowing for a higher fraction of the larger $(Ga_{1-x}Zn_x)(N_{1-x}O_x)$ particles in the final product.

The discrepancy between the compositions at the ensemble and the individual particle level decreases with increasing nitridation temperature. A comparison of ensemble x values and composition of individual particles for the set of samples in Figure 5 is shown in Table 2. EDS quantitative analysis of the large particles from those samples is shown in Figure S19. In the case of the 650 and 700 °C syntheses, large particles have higher x values (*i.e.*, higher Zn content) than the ensemble composition. However, the 750 and 800 °C syntheses produce particles that individually have compositions that match the ensemble x value. We note that the small aggregated particles are not observed in samples synthesized at 750 and 800 °C. Our results suggest that the higher-temperature synthesis leads to samples that consist of only the large wurtzite $(Ga_{1-x}Zn_x)(N_{1-x}O_x)$ NCs that have fairly homogeneous elemental distributions.

Table 2. Summary of x Values in $(Ga_{1-x}Zn_x)(N_{1-x}O_x)$ NCs Synthesized at 650, 700, 750, and 800 °C Determined by ICP-OES and EDS Elemental Analyses

	composition, x	
temperature (°C)	ICP-OES (ensemble)	EDS quantification (single particle)
650	0.38 ± 0.00	0.85 ± 0.04
700	0.36 ± 0.01	0.66 ± 0.11
750	0.37 ± 0.02	0.40 ± 0.05
800	0.35 ± 0.01	0.33 ± 0.05
800	0.11 ± 0.01	0.13 ± 0.02
800	0.21 ± 0.01	0.23 ± 0.03
800	0.44 ± 0.01	0.43 ± 0.04

The XRD patterns of samples of similar ensemble composition (x ~0.35) made at different temperatures (Figure 5) are consistent with this picture. Samples synthesized at higher temperatures have decreasing amounts of the broad background that we attribute to nitrided $ZnGa_2O_4$ (Figure S6). Although the samples have similar ensemble compositions, we observe a shift of the wurtzite peaks toward the higher diffraction angle (toward GaN) in the samples produced at higher reaction temperature. The lattice constants a and c of the 800 °C product decrease by ~0.51% and 0.22%, respectively (see Figure S6) compared to those of the 650 °C sample. This shift is consistent with the fact that the large wurtzite particles represented by the XRD patterns have lower x values (*i.e.*, less Zn) when made at higher temperatures.

The match in composition between the $(Ga_{1-x}Zn_x)(N_{1-x}O_x)$ ensemble sample and individual particles is confirmed in the series of samples synthesized at 800 °C shown in Figure 6 (Table 2). Average x values obtained from the EDS compositional analyses on the products of the 10, 6, 4, and 3 h reactions are 0.13 ± 0.02, 0.23 ± 0.03, 0.33 ± 0.05 and 0.43 ± 0.04, respectively, as shown in Figure S20. The x values are obtained by averaging at least 16 particles per sample. They are in good agreement with ensemble x values (0.11, 0.21, 0.35 and 0.44) as analyzed by ICP-OES. These results confirm that bulk composition is reflected in individual $(Ga_{1-x}Zn_x)(N_{1-x}O_x)$ particles synthesized at the higher temperatures.

DISCUSSION

The results described above show that nitridation temperature controls the elemental distribution in samples of $(Ga_{1-x}Zn_x)(N_{1-x}O_x)$ NCs. We previously reported that the lowest nitridation temperature at which spinel $ZnGa_2O_4$ signals in the XRD disappear and only wurtzite $(Ga_{1-x}Zn_x)(N_{1-x}O_x)$ peaks are clearly visible is 650 °C.[23] The data above demonstrates that, at this reaction temperature, the product is highly heterogeneous, consisting of wurtzite $(Ga_{1-x}Zn_x)(N_{1-x}O_x)$ single crystals with Ga and N enrichment near the surface and small aggregated particles of ambiguous crystal structure. The wurtzite particles have high x values, 0.8−0.9. The remaining Ga and N that make up the ensemble x value measured by ICP-OES come from the small particles. The x values of individual particles match the ensemble x value at 750 °C and above. At those higher temperatures, we no longer observe the presence of the small aggregated particles. We also observe increasingly correlated elemental distribution within each particle with increasing temperature. The Kubelka−Munk absorption spectra of the samples synthesized at 800 °C show the absorption edges in the visible region and the band gap energy that decreases with increasing x values. Taken together, these observations allow us to propose the formation mechanism of the NCs at 650 and 800 °C and examine the effects of experimental conditions on optical properties.

Formation Mechanism as a Function of Temperature. The results described above provide us with an improved understanding of the mechanism behind $(Ga_{1-x}Zn_x)(N_{1-x}O_x)$ NC formation. The essential steps of the mechanism that we propose are schematically illustrated in Scheme 1. We first describe the formation mechanism of the large wurtzite NCs synthesized at 650 °C, which exhibit Ga and N enrichment near the surface (Figure 2 and 3). In the beginning of the nitridation reaction, the starting materials, ZnO and $ZnGa_2O_4$ NCs, appear to fuse together, as demonstrated in our previous report.[24] This happens within 0−2 h at 650 °C.[24] Reaction with NH_3, phase transformation of cubic spinel $ZnGa_2O_4$ (on the ZnO surface) to wurtzite, and the diffusion of the elements within the fused particles occur to create the $(Ga_{1-x}Zn_x)(N_{1-x}O_x)$ NCs. The decomposition of NH_3 requires a temperature slightly below 500 °C.[42,43] A wide range of molecular or radical nitrogen-containing intermediates such as NH, NH_2[44] and N_2H_4[45] are possibly released[46] and react with the particles. The diffusion of nitrogen is probably driven by Ga since they are trivalent and valence-matched (Ga^{3+} and N^{3-}).[47−49] Diffusion in solids occurs over surfaces and along grain boundaries more rapidly than through the interiors of the crystal.[50] As a consequence, at

DOI: 10.1021/acsnano.7b03891
ACS Nano 2017, 11, 8401−8412

Scheme 1. Proposed Mechanism for the Formation of $(Ga_{1-x}Zn_x)(N_{1-x}O_x)$ NCs Obtained from the Nitridation of a Mixture of $ZnGa_2O_4$ and ZnO NCs at 650 and 800 °C[a]

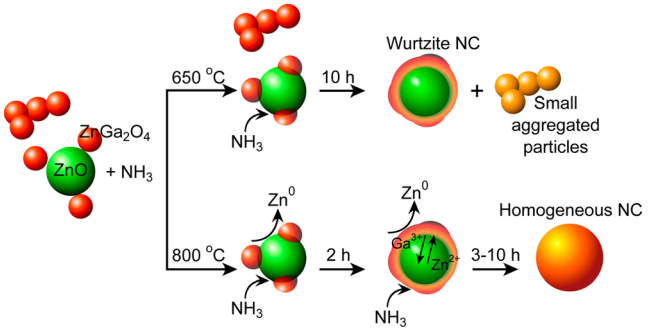

[a]At 650 °C, the wurtzite NCs along with small aggregated particles are obtained, while the reaction at 800 °C produces homogeneous wurtzite NCs.

650 °C, the combination of the reaction with nitrogen and the diffusion of Zn^{2+} and Ga^{3+} within fused ZnO/$ZnGa_2O_4$ NCs is concentrated in the interface and surface areas, resulting in Ga-rich outer regions and Zn-rich cores (see Figure 2). EDS mapping shows similar results if reaction time is prolonged to 16 h (see Figure S21). We note that we do not see evidence of phase separated pure GaN and ZnO. We also note that hydrogen incorporation is possible during decomposition of NH_3.[51] However, hydrogen incorporation causes a lattice expansion in ZnO,[52,53] which is not apparent in our XRD patterns (Figures S1 and S6).

The proposed mechanism for the formation of the small aggregated particles at 650 °C is also shown in Scheme 1. These particles are formed by the reaction of NH_3 gas and $ZnGa_2O_4$ NCs that are not in contact with ZnO NCs because they are not perfectly mixed in the solid state. Previous studies show that the complete conversion of cubic spinel $ZnGa_2O_4$ alone to unambiguous wurtzite $(Ga_{1-x}Zn_x)(N_{1-x}O_x)$ requires the nitridation temperature of at least 750 °C for nanoparticles[24] and 850 °C for bulk.[54] The small aggregated particles made at 650 °C have broad peaks in the XRD, making it difficult to unambiguously determine their crystal structure (see Figure 8c). They may be spinel, wurtzite, or a mixture of the two. These particles contain Ga, N, Zn, and O with a homogeneous distribution shown by EDS mapping (see Figure 8d). Homogeneous incorporation of nitrogen is possibly due to the small size of $ZnGa_2O_4$ NCs (diameter ~5 nm), making for shorter diffusion distances.

The formation mechanism of homogeneous $(Ga_{1-x}Zn_x)(N_{1-x}O_x)$ NCs at 800 °C is also illustrated in Scheme 1. The processes include the fusing of the starting materials, $ZnGa_2O_4$ and ZnO NCs, similar to the process at 650 °C, and phase transformation and diffusion of elements within the particle along with reaction with NH_3. Within 2 h, the NCs enriched in Zn and O at the particle core and Ga and N near the surface are formed, revealed by STEM-EDS mapping shown in Figure S9. Prolonging the reaction time for another hour leads to NCs with highly correlated elemental distributions. The increase in homogeneity for the products synthesized at 800 °C may be due to several factors. First, the decomposition of NH_3 is faster at 800 °C compared to 650 °C[43] resulting in the larger amount of nitrogen-containing species released into the reaction. Second, the diffusion coefficients of Zn and Ga in ZnO increase with temperature.[55−57] By increasing the nitridation temperature from 650 to 800 °C, an increase in the diffusion depth of the elements can be expected. Third, the evaporation of Zn^0 from the particles at temperatures above 650 °C likely creates defects such as Zn vacancy sites. Diffusion of Zn^{2+} and Ga^{3+} from and into the ZnO particle may occur through a Zn vacancy-assisted mechanism.[56−60] The vacancy-assisted diffusion of Ga^{3+} can increase the amount and depth of Ga incorporated into the ZnO starting material NCs. The combination of these factors results in control of elemental distribution in $(Ga_{1-x}Zn_x)(N_{1-x}O_x)$ NCs with a range of homogeneity that depends on temperature.

Optical Properties of $(Ga_{1-x}Zn_x)(N_{1-x}O_x)$ NCs Synthesized at 650 and 800 °C. As the composition-dependent band gap energies are the signature feature of $(Ga_{1-x}Zn_x)(N_{1-x}O_x)$ materials, we now turn to the discussion of optical properties of our $(Ga_{1-x}Zn_x)(N_{1-x}O_x)$ products. The absorption spectra of the $(Ga_{1-x}Zn_x)(N_{1-x}O_x)$ NCs synthesized at 650 °C have been described previously.[23,24] The absorption spectra shown in Figure 7 for samples synthesized at 800 °C are qualitatively similar in terms of spectral shape and extension of the absorption into the visible range, suggesting that the elemental distribution in these materials makes a subtle, rather than drastic, difference in their optical properties. The absorption onset in samples synthesized at 800 °C red-shifts with increasing ZnO content (see Figure 7). This trend was also observed in nano-[27] and bulk-scale[13,61] $(Ga_{1-x}Zn_x)(N_{1-x}O_x)$ solid solutions obtained at high temperatures (≥800 °C) reported elsewhere. Theoretical work has predicted that band gap energies at constant composition should decrease with increasing synthesis temperatures due to increasing compositional homogeneity.[30] Unfortunately, we cannot directly compare band gaps as a function of temperature because we do not have samples where the large wurtzite particles synthesized at 800 and 650 °C have the same x values. The 800 °C samples are homogeneous in composition so the ensemble x value reflects the composition of individual particles, but our x values are only as high as 0.44. In the 650 °C samples, there is heterogeneity in both composition and elemental distribution among particles and the large wurtzite $(Ga_{1-x}Zn_x)(N_{1-x}O_x)$ NCs have high x values (~0.8−0.9). For this reason, we are not able to directly assess the effect of increased homogeneity on the band gap of $(Ga_{1-x}Zn_x)(N_{1-x}O_x)$ NCs. For similar reasons, we cannot directly compare XRD patterns of $(Ga_{1-x}Zn_x)(N_{1-x}O_x)$ samples made at the two temperatures.

Perhaps a more interesting question is what determines the band gap values in the samples synthesized at 650 °C and what explains their variation with ensemble x value. The observed absorption onsets range from 477 to 565 nm with ensemble compositions varying from x = 0.42 to x = 0.87.[23,24] Since the product of 650 °C is composed of two types of particles (small aggregated and large wurtzite particles), both of which absorb in the visible, it is possible that the absorption spectrum contains contributions from both types of particles so that their ratio leads to the change of the band gaps with ensemble compositions. To evaluate the plausibility of this hypothesis, we simulated absorption spectra using linear combinations of the experimental spectra of the nitrided $ZnGa_2O_4$ (x = 0.21) and the $(Ga_{1-x}Zn_x)(N_{1-x}O_x)$ NCs (x = 0.87), both made at 650 °C (Figure 9a). We chose these particular samples as model spectra because the former are representative of the small aggregated particles and the latter represents the large wurtzite particles. Resulting simulated spectra, shown in Figure 9b, show

DOI: 10.1021/acsnano.7b03891
ACS Nano 2017, 11, 8401−8412

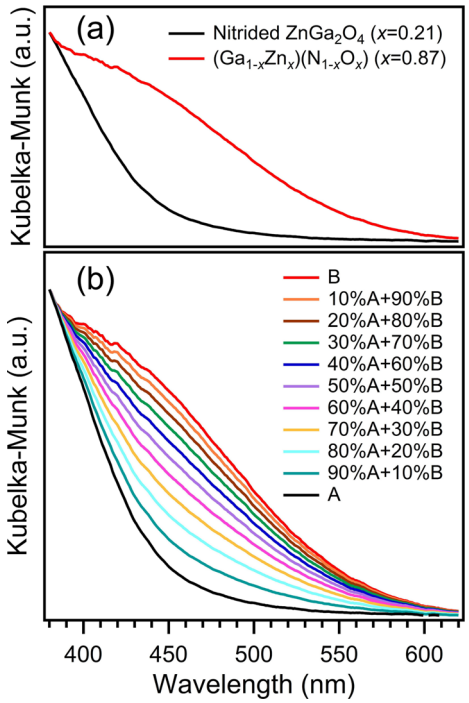

Figure 9. (a) Kubelka–Munk absorption spectra of the nitrided $ZnGa_2O_4$ (x = 0.21; A) (black trace) and the $(Ga_{1-x}Zn_x)(N_{1-x}O_x)$ NCs (x = 0.87) (red trace). The spectra are normalized at 380 nm. (b) Simulated Kubelka–Munk absorption spectra of the $(Ga_{1-x}Zn_x)(N_{1-x}O_x)$ NCs with different compositions. The simulated spectra are generated using linear combinations of experimental spectra of the nitrided $ZnGa_2O_4$ (x = 0.21; A) and the $(Ga_{1-x}Zn_x)(N_{1-x}O_x)$ NCs (x = 0.87; B). The spectra are normalized at 380 nm.

that indeed the absorption shifts further to the red as the ratio of large wurtzite to small aggregated particles increases. This result suggests that it is possible for varying ratios of the two types of species to shift the apparent band gap. However, the shapes of the simulated spectra do not quite match the experimental spectra,[23,24] suggesting that the situation is not quite so simple. It is likely that distributions in the compositions of the large as well as small particles can broaden the transitions such that a simple sum of two representative spectra does not describe each ensemble x value sufficiently well. It remains to be seen exactly what determines the composition-dependent spectra of samples synthesized at 650 °C and the corresponding wide range of apparent band gaps and, ultimately, what role elemental distribution may play in the efficiency of photochemical water splitting.

CONCLUSIONS

In summary, we have shown that the elemental distribution in samples of $(Ga_{1-x}Zn_x)(N_{1-x}O_x)$ NCs produced using a mixture of ZnO and $ZnGa_2O_4$ NCs is controlled by nitridation temperature. At 650 °C, the product is highly heterogeneous, consisting of wurtzite single-crystalline $(Ga_{1-x}Zn_x)(N_{1-x}O_x)$ particles with Ga and N enrichment near the surface and small aggregated particles of ambiguous crystal structure. The wurtzite NCs have high x values, 0.8–0.9, which do not match the ensemble x values measured by ICP-OES because most of the Ga and N come from the small aggregated particles. With increasing temperature, the elemental distribution is increasingly more homogeneous and the x values of individual particles eventually match the ensemble x value. We propose a mechanism responsible for the formation of $(Ga_{1-x}Zn_x)(N_{1-x}O_x)$ NCs at 650 and 800 °C. The formation mechanism involves phase transformation, nitridation, and diffusion of the constituent elements. At 650 °C, the latter two steps are concentrated near the surface, resulting in particles with Ga and N enrichment there. By increasing the nitridation temperature to 800 °C, particles with homogeneously distributed elements are achieved. We observe a decrease in band gap energy with increasing x values in the homogeneous $(Ga_{1-x}Zn_x)(N_{1-x}O_x)$ NCs, qualitatively similar to what has been observed for the material made at 650 °C. The exact role of elemental distribution in determining optical and photochemical properties remains to be determined.

MATERIALS AND METHODS

Chemicals. Zinc acetylacetonate hydrate [$Zn(acac)_2$, 99.995%], gallium acetylacetonate [$Ga(acac)_3$, 99.99%], 1,2-hexadecanediol (90%), oleic acid (≥99.0%), oleylamine (70%), benzyl ether (98%), zinc chloride ($ZnCl_2$, ≥98%), 3-mercaptopropionic acid (3-MPA, ≥ 99.0%), tetramethylammonium hydroxide pentahydrate (≥97%), hexane (99%) and toluene (99.5%) were purchased from Sigma-Aldrich. Sodium hydroxide (NaOH pellets, 99.3%), 2-propanol (99.9%) and methanol (99.9%) were purchased from Fisher Scientific. 1,2-Ethanediol (99.8%) was purchased from Macron Fine Chemicals. Ethanol (95%) was purchased from Decon Laboratories. Ammonia (99.99%) was purchased from Airgas. All chemicals were purchased commercially and used without further purification.

$(Ga_{1-x}Zn_x)(N_{1-x}O_x)$ NC Synthesis. The $(Ga_{1-x}Zn_x)(N_{1-x}O_x)$ NCs were synthesized as described previously.[23,24] Typically, a powder mixture of ZnO and 3-MPA capped $ZnGa_2O_4$ NCs were dispersed in a water/ethanol mixture (50/50 by volume) and dried on a glass slide. The dry mixture was then transferred to an alumina boat and placed into the hot zone of a quartz tube furnace. All nitridation reactions were carried out in a tube furnace (Across International model STF 1200). Prior to nitridation, the tube furnace (with the starting mixture) was purged with argon for 1 h followed by NH_3 gas for 30 min at room temperature. Subsequently, the temperature was raised to 650 °C with a ramp up speed of 20 °C min^{-1} under NH_3 flow (~150 mL min^{-1}). The starting materials were nitrided for 10 h. Upon completion of nitridation, the furnace was allowed to cool down to room temperature with flowing NH_3 and flushed with Ar before removal of the nitrided products. Resultant products were stored in a small vial for further use. For nitridation temperature dependence experiments, the nitrided products were obtained by varying nitridation reaction temperatures: 700, 750, 800, 850, and 900 °C with 10 h reaction time. The different compositions, x, in the products prepared at 800 °C nitridation temperature were controlled by varying nitridation reaction times: 2, 3, 4, 6, and 10 h.

Characterization and Elemental Analysis. Powder XRD patterns were collected on a Rigaku Dmax diffractometer using a Cu Kα radiation source (λ = 0.1540562 nm). The patterns were recorded from 25 to 85° 2θ using a step size of 0.02° 2θ. Diffuse reflectance spectra were collected on a Shimadzu UV-3600 spectrophotometer equipped with an integrating sphere. Diffuse reflectance was converted to a Kubelka–Munk plot using the equation $[F(R_\infty) = (1 - R_\infty)^2/2R_\infty; R_\infty = R_{sample}/R_{reference}]$. $BaSO_4$ was used as a reference material to obtain the reflectance of reference ($R_{reference}$). Elemental analysis of Zn and Ga was carried out using an ARL 3410+ ICP-OES. For transmission electron microscopy studies, the samples were prepared by dropping dilute suspensions of NCs onto ultrathin carbon coated copper grids and by picking up dry powder on lacey carbon film supported by copper 300 mesh grids. Bright-field TEM imaging was carried out on Tecnai T12 Spirit, Tecnai G2 and Tecnai ST30 FEI microscopes operated at 100–300 kV. ADF and HAADF-STEM images were obtained using FEI Titan and FEI Talos F200X microscopes operated at 80–200 kV. The STEM convergence semiangle was 10 mrad with 100–250 (FEI Titan) and 50–150

DOI: 10.1021/acsnano.7b03891
ACS Nano 2017, 11, 8401–8412

(FEI Talos) mrad HAADF detector inner semiangle. STEM-EDS experiments were performed on FEI Titan and FEI Talos F200X microscopes, equipped with a Super-X EDS system (four silicon drift detectors, SDDs), and operated at 80 and 200 kV, respectively. STEM-EDS data analysis was performed using Bruker Esprit software.

EDS Elemental Map Processing. EDS elemental maps were processed and quantified using Bruker Esprit software as described previously.[32] Briefly, the Bremsstrahlung background X-rays was fitted and subtracted from the hyperspectral elemental maps. The detector effects were removed from the spectra by applying the correction for escape peaks, shelf, pileup peaks, shift and tail errors. A peak deconvolution using Bayes model was performed to remove contribution from the Cu from the spectra which could come from the grids. The Cliff-Lorimer method was used for elemental quantification and the elemental compositions were determined by integrating the peak of N−Kα, O−Kα, Zn−Kα and Ga−Kα at 0.39, 0.52, 8.63, and 9.24 keV, respectively.

Scatter Plot and Colocation Analysis. The EDS elemental maps processed and quantified as described above were exported from the Bruker Esprit software. The Zn and Ga maps were exported separately as color-coded images, with green and red colors representing Zn and Ga, respectively. The pixel intensities were scaled linearly with X-ray counts for the representative elements. The images were converted to 8-bit in ImageJ software, where the intensity was scaled from 0 to 255. A Gaussian filter with a sigma (σ) value of 1 was applied to each map to interpolate the discrete X-ray counts. A scatter plot of Zn and Ga intensities was generated and statistical analysis of element spatial association was performed using a Fiji plugin, ScatterJ.[62] The spatial correlation of Zn and Ga was quantified using the Pearson's r, which characterizes the linear correlation between two variables and was calculated according to the expression below:[35]

$$\text{Pearson's } r = \frac{1}{(N-1)} \sum_{i=1}^{N} \left(\frac{r_i - \overline{r}}{S_r} \right) \left(\frac{g_i - \overline{g}}{S_g} \right) \quad (1)$$

where N is the total number of pixels in the combined elemental map (Zn and Ga); r_i and g_i are to the intensity values of the Ga and Zn, respectively, across the entire image, of pixel i; $\overline{r}$ and $\overline{g}$ refer to the mean intensities of the Ga and Zn, respectively, and s_r and s_g are the sample standard deviations of the Ga and Zn, respectively.

ASSOCIATED CONTENT

Supporting Information

The Supporting Information is available free of charge on the ACS Publications website at DOI: 10.1021/acsnano.7b03891.

Figures S1−S21 and Tables S1−S2 (PDF)

AUTHOR INFORMATION

Corresponding Author

*E-mail: gordana.dukovic@colorado.edu.

ORCID

Gordana Dukovic: 0000-0001-5102-0958

Present Addresses

§Thermo Fisher Scientific, 5350 NE Dawson Creek Drive, Hillsboro, Oregon 97124, United States.

∥Basic Materials and Chemicals, LG Chem Research Park, LG Chem, Daejeon 34122, Korea.

Notes

The authors declare no competing financial interest.

ACKNOWLEDGMENTS

This work was supported primarily by a Beckman Young Investigator Award from the Arnold and Mabel Beckman Foundation. Support was also provided by the Cottrell Scholar Award from Research Corporation for Science Advancement. STEM-EDS measurements were carried out at the National Center for Electron Microscopy facility of the Molecular Foundry at Lawrence Berkeley National Laboratory, supported by the Office of Science, Office of Basic Energy Sciences, of the U.S. Department of Energy under Contract No. DE-AC02-05CH11231 and at the Colorado School of Mines Electron Microscopy Laboratory. TEM image in Figure 1 was taken at the CAMCOR facility at the University of Oregon. We thank James Utterback and Orion Pearce for helpful discussions.

REFERENCES

(1) Osterloh, F. E. Inorganic Materials as Catalysts for Photochemical Splitting of Water. *Chem. Mater.* **2008**, *20*, 35−54.

(2) Kudo, A.; Miseki, Y. Heterogeneous Photocatalyst Materials for Water Splitting. *Chem. Soc. Rev.* **2009**, *38*, 253−278.

(3) Ibanez, M.; Zamani, R.; Li, W.; Shavel, A.; Arbiol, J.; Morante, J. R.; Cabot, A. Extending the Nanocrystal Synthesis Control to Quaternary Compositions. *Cryst. Growth Des.* **2012**, *12*, 1085−1090.

(4) Aldakov, D.; Lefrancois, A.; Reiss, P. Ternary and Quaternary Metal Chalcogenide Nanocrystals: Synthesis, Properties and Applications. *J. Mater. Chem. C* **2013**, *1*, 3756−3776.

(5) Fan, F.-J.; Wu, L.; Yu, S.-H. Energetic I-III-VI_2 and I_2-II-IV-VI_4 Nanocrystals: Synthesis, Photovoltaic and Thermoelectric Applications. *Energy Environ. Sci.* **2014**, *7*, 190−208.

(6) Kuykendall, T.; Ulrich, P.; Aloni, S.; Yang, P. Complete Composition Tunability of InGaN Nanowires Using a Combinatorial Approach. *Nat. Mater.* **2007**, *6*, 951−956.

(7) Buscaglia, M. T.; Harnagea, C.; Dapiaggi, M.; Buscaglia, V.; Pignolet, A.; Nanni, P. Ferroelectric $BaTiO_3$ Nanowires by a Topochemical Solid-State Reaction. *Chem. Mater.* **2009**, *21*, 5058−5065.

(8) Buscaglia, M. T.; Sennour, M.; Buscaglia, V.; Bottino, C.; Kalyani, V.; Nanni, P. Formation of $Bi_4Ti_3O_{12}$ One-Dimensional Structures by Solid-State Reactive Diffusion. From Core−Shell Templates to Nanorods and Nanotubes. *Cryst. Growth Des.* **2011**, *11*, 1394−1401.

(9) He, X.; Wang, J.; Dai, Z.; Wang, L.; Tian, G. The Synthesis of $LiMn_xFe_{1-x}PO_4$/C Cathode Material through Solvothermal Jointed with Solid-State Reaction. *Materials* **2016**, *9*, 766.

(10) Maeda, K.; Takata, T.; Hara, M.; Saito, N.; Inoue, Y.; Kobayashi, H.; Domen, K. GaN:ZnO Solid Solution as a Photocatalyst for Visible-Light-Driven Overall Water Splitting. *J. Am. Chem. Soc.* **2005**, *127*, 8286−8287.

(11) Maeda, K.; Teramura, K.; Takata, T.; Hara, M.; Saito, N.; Toda, K.; Inoue, Y.; Kobayashi, H.; Domen, K. Overall Water Splitting on $(Ga_{1-x}Zn_x)(N_{1-x}O_x)$ Solid Solution Photocatalyst: Relationship between Physical Properties and Photocatalytic Activity. *J. Phys. Chem. B* **2005**, *109*, 20504−20510.

(12) Maeda, K.; Teramura, K.; Lu, D.; Takata, T.; Saito, N.; Inoue, Y.; Domen, K. Photocatalyst Releasing Hydrogen from Water. *Nature* **2006**, *440*, 295.

(13) Maeda, K.; Domen, K. Solid Solution of GaN and ZnO as a Stable Photocatalyst for Overall Water Splitting under Visible Light. *Chem. Mater.* **2010**, *22*, 612−623.

(14) Maeda, K.; Teramura, K.; Lu, D.; Takata, T.; Saito, N.; Inoue, Y.; Domen, K. Characterization of Rh-Cr Mixed-Oxide Nanoparticles Dispersed on $(Ga_{1-x}Zn_x)(N_{1-x}O_x)$ as a Cocatalyst for Visible-Light-Driven Overall Water Splitting. *J. Phys. Chem. B* **2006**, *110*, 13753−13758.

(15) Maeda, K.; Teramura, K.; Saito, N.; Inoue, Y.; Domen, K. Improvement of Photocatalytic Activity of $(Ga_{1-x}Zn_x)(N_{1-x}O_x)$ Solid Solution for Overall Water Splitting by Co-loading Cr and Another Transition Metal. *J. Catal.* **2006**, *243*, 303−308.

(16) Maeda, K.; Teramura, K.; Masuda, H.; Takata, T.; Saito, N.; Inoue, Y.; Domen, K. Efficient Overall Water Splitting under Visible-Light Irradiation on $(Ga_{1-x}Zn_x)(N_{1-x}O_x)$ Dispersed with Rh−Cr Mixed-Oxide Nanoparticles: Effect of Reaction Conditions on Photocatalytic Activity. *J. Phys. Chem. B* **2006**, *110*, 13107−13112.

DOI: 10.1021/acsnano.7b03891
ACS Nano 2017, 11, 8401−8412

(17) Maeda, K.; Domen, K. New Non-Oxide Photocatalysts Designed for Overall Water Splitting under Visible Light. *J. Phys. Chem. C* **2007**, *111*, 7851−7861.
(18) Maeda, K.; Hashiguchi, H.; Masuda, H.; Abe, R.; Domen, K. Photocatalytic Activity of $(Ga_{1-x}Zn_x)(N_{1-x}O_x)$ for Visible-Light-Driven H_2 and O_2 Evolution in the Presence of Sacrificial Reagents. *J. Phys. Chem. C* **2008**, *112*, 3447−3452.
(19) Maeda, K.; Teramura, K.; Domen, K. Effect of Post-Calcination on Photocatalytic Activity of $(Ga_{1-x}Zn_x)(N_{1-x}O_x)$ Solid Solution for Overall Water Splitting under Visible Light. *J. Catal.* **2008**, *254*, 198−204.
(20) Hisatomi, T.; Maeda, K.; Lu, D.; Domen, K. The Effects of Starting Materials in the Synthesis of $(Ga_{1-x}Zn_x)(N_{1-x}O_x)$ Solid Solution on Its Photocatalytic Activity for Overall Water Splitting under Visible Light. *ChemSusChem* **2009**, *2*, 336−343.
(21) Hisatomi, T.; Maeda, K.; Takanabe, K.; Kubota, J.; Domen, K. Aspects of the Water Splitting Mechanism on $(Ga_{1-x}Zn_x)(N_{1-x}O_x)$ Photocatalyst Modified with $Rh_{2-y}Cr_yO_3$ Cocatalyst. *J. Phys. Chem. C* **2009**, *113*, 21458−21466.
(22) Ohno, T.; Bai, L.; Hisatomi, T.; Maeda, K.; Domen, K. Photocatalytic Water Splitting Using Modified GaN:ZnO Solid Solution under Visible Light: Long-Time Operation and Regeneration of Activity. *J. Am. Chem. Soc.* **2012**, *134*, 8254−8259.
(23) Lee, K.; Tienes, B. M.; Wilker, M. B.; Schnitzenbaumer, K. J.; Dukovic, G. $(Ga_{1-x}Zn_x)(N_{1-x}O_x)$ Nanocrystals: Visible Absorbers with Tunable Composition and Absorption Spectra. *Nano Lett.* **2012**, *12*, 3268−3272.
(24) Lee, K.; Lu, Y.-G.; Chuang, C.-H.; Ciston, J.; Dukovic, G. Synthesis and Characterization of $(Ga_{1-x}Zn_x)(N_{1-x}O_x)$ Nanocrystals with a Wide Range of Compositions. *J. Mater. Chem. A* **2016**, *4*, 2927−2935.
(25) Mapa, M.; Thushara, K. S.; Saha, B.; Chakraborty, P.; Janet, C. M.; Viswanath, R. P.; Nair, C. M.; Murty, K. V. G. K.; Gopinath, C. S. Electronic Structure and Catalytic Study of Solid Solution of GaN in ZnO. *Chem. Mater.* **2009**, *21*, 2973−2979.
(26) Chen, H.; Wang, L.; Bai, J.; Hanson, J. C.; Warren, J. B.; Muckerman, J. T.; Fujita, E.; Rodriguez, J. A. *In Situ* XRD Studies of ZnO/GaN Mixtures at High Pressure and High Temperature: Synthesis of Zn-Rich $(Ga_{1-x}Zn_x)(N_{1-x}O_x)$ Photocatalysts. *J. Phys. Chem. C* **2010**, *114*, 1809−1814.
(27) Wang, J.; Huang, B.; Wang, Z.; Wang, P.; Cheng, H.; Zheng, Z.; Qin, X.; Zhang, X.; Dai, Y.; Whangbo, M.-H. Facile Synthesis of Zn-rich $(GaN)_{1-x}(ZnO)_x$ Solid Solutions Using Layered Double Hydroxides as Precursors. *J. Mater. Chem.* **2011**, *21*, 4562−4567.
(28) Reinert, A. A.; Payne, C.; Wang, L.; Ciston, J.; Zhu, Y.; Khalifah, P. G. Synthesis and Characterization of Visible Light Absorbing $(GaN)_{1-x}(ZnO)_x$ Semiconductor Nanorods. *Inorg. Chem.* **2013**, *52*, 8389−8398.
(29) Chen, D. P.; Skrabalak, S. E. Synthesis of $(Ga_{1-x}Zn_x)(N_{1-x}O_x)$ with Enhanced Visible-Light Absorption and Reduced Defects by Suppressing Zn Volatilization. *Inorg. Chem.* **2016**, *55*, 3822−3828.
(30) Wang, S.; Wang, L.-W. Atomic and Electronic Structures of GaN/ZnO Alloys. *Phys. Rev. Lett.* **2010**, *104*, 065501.
(31) Li, L.; Muckerman, J. T.; Hybertsen, M. S.; Allen, P. B. Phase Diagram, Structure, and Electronic Properties of $(Ga_{1-x}Zn_x)(N_{1-x}O_x)$ Solid Solutions from DFT-Based Simulations. *Phys. Rev. B* **2011**, *83*, 134202.
(32) Johnson, G. R.; Werner, S.; Bustillo, K. C.; Ercius, P.; Kisielowski, C.; Bell, A. T. Investigations of Element Spatial Correlation in Mn-Promoted Co-Based Fischer−Tropsch Synthesis Catalysts. *J. Catal.* **2015**, *328*, 111−122.
(33) Schmid, G.; Zeitvogel, F.; Hao, L.; Ingino, P.; Adaktylou, I.; Eickhoff, M.; Obst, M. Submicron-Scale Heterogeneities in Nickel Sorption of Various Cell-Mineral Aggregates Formed by Fe(II)-Oxidizing Bacteria. *Environ. Sci. Technol.* **2016**, *50*, 114−125.
(34) Taylor, R. Interpretation of the Correlation Coefficient: A Basic Review. *J. Diagn. Med. Sonogr.* **1990**, *6*, 35−39.
(35) Pearson, K. Mathematical Contributions to the Theory of Evolution. III. Regression, Heredity, and Panmixia. *Philos. Trans. R. Soc. London, A* **1896**, *187*, 253−318.
(36) Han, W.-Q.; Liu, Z.; Yu, H.-G. Synthesis and Optical Properties of GaN/ZnO Solid Solution Nanocrystals. *Appl. Phys. Lett.* **2010**, *96*, 183112.
(37) Feygenson, M.; Neuefeind, J. C.; Tyson, T. A.; Schieber, N.; Han, W.-Q. Average and Local Crystal Structures of $(Ga_{1-x}Zn_x)$-$(N_{1-x}O_x)$ Solid Solution Nanoparticles. *Inorg. Chem.* **2015**, *54*, 11226−11235.
(38) Jensen, L. L.; Muckerman, J. T.; Newton, M. D. First-Principles Studies of the Structural and Electronic Properties of the $(Ga_{1-x}Zn_x)$-$(N_{1-x}O_x)$ Solid Solution Photocatalyst. *J. Phys. Chem. C* **2008**, *112*, 3439−3446.
(39) Li, Y.; Zhu, L.; Yang, Y.; Song, H.; Lou, Z.; Guo, Y.; Ye, Z. A Full Compositional Range for a $(Ga_{1-x}Zn_x)(N_{1-x}O_x)$ Nanostructure: High Efficiency for Overall Water Splitting and Optical Properties. *Small* **2015**, *11*, 871−876.
(40) Ram Boppana, V. B.; Doren, D. J.; Lobo, R. F. Analysis of Ga Coordination Environment in Novel Spinel Zinc Gallium Oxy-nitride Photocatalysts. *J. Mater. Chem.* **2010**, *20*, 9787−9797.
(41) Ram Boppana, V. B.; Schmidt, H.; Jiao, F.; Doren, D. J.; Lobo, R. F. Structure Analysis and Photocatalytic Properties of Spinel Zinc Gallium Oxonitrides. *Chem. - Eur. J.* **2011**, *17*, 12417−12428.
(42) Perman, E. P.; Atkinson, G. A. S. The Decomposition of Ammonia by Heat. *Proc. R. Soc. London* **1904**, *74*, 110−117.
(43) White, A. H.; Melville, W. The Decomposition of Ammonia at High Temperatures. *J. Am. Chem. Soc.* **1905**, *27*, 373−386.
(44) Rahinov, I.; Ditzian, N.; Goldman, A.; Cheskis, S. NH_2 Radical Formation by Ammonia Pyrolysis in a Temperature Range of 800−1000 K. *Appl. Phys. B* **2003**, *77*, 541−546.
(45) Dirtu, D.; Odochian, L.; Pui, A.; Humelnicu, I. Thermal Decomposition of Ammonia. N_2H_4 - an Intermediate Reaction Product. *Cent. Eur. J. Chem.* **2006**, *4*, 666−673.
(46) Chen, H.; Nambu, A.; Wen, W.; Graciani, J.; Zhong, Z.; Hanson, J. C.; Fujita, E.; Rodriguez, J. A. Reaction of NH_3 with Titania: N-Doping of the Oxide and TiN Formation. *J. Phys. Chem. C* **2007**, *111*, 1366−1372.
(47) Yamamoto, T.; Katayama-Yoshida, H. Solution Using a Codoping Method to *Unipolarity* for the Fabrication of *p*-Type ZnO. *Jpn. J. Appl. Phys.* **1999**, *38*, L166−L169.
(48) Matsui, H.; Saeki, H.; Tabata, H.; Kawai, T. Role of Ga for Co-doping of Ga with N in ZnO Films. *Jpn. J. Appl. Phys.* **2003**, *42*, 5494−5499.
(49) Ahn, K.-S.; Yan, Y.; Shet, S.; Deutsch, T.; Turner, J.; Al-Jassim, M. Enhanced Photoelectrochemical Responses of ZnO Films Through Ga and N Codoping. *Appl. Phys. Lett.* **2007**, *91*, 231909.
(50) Fisher, J. C. Calculation of Diffusion Penetration Curves for Surface and Grain Boundary Diffusion. *J. Appl. Phys.* **1951**, *22*, 74−77.
(51) Baumvol, I. J. R.; Stedile, F. C.; Ganem, J.-J.; Trimaille, I.; Rigo, S. Thermal Nitridation of SiO_2 Films in Ammonia: The Role of Hydrogen. *J. Electrochem. Soc.* **1996**, *143*, 1426−1434.
(52) Chen, L.-Y.; Chen, W.-H.; Wang, J.-J.; Hong, F. C.-N.; Su, Y.-K. Hydrogen-Doped High Conductivity ZnO Films Deposited by Radio-Frequency Magnetron Sputtering. *Appl. Phys. Lett.* **2004**, *85*, 5628−5630.
(53) Van de Walle, C. G. Hydrogen as a Cause of Doping in Zinc Oxide. *Phys. Rev. Lett.* **2000**, *85*, 1012−1015.
(54) Chen, H.; Wen, W.; Wang, Q.; Hanson, J. C.; Muckerman, J. T.; Fujita, E.; Frenkel, A. I.; Rodriguez, J. A. Preparation of $(Ga_{1-x}Zn_x)$-$(N_{1-x}O_x)$ Photocatalysts from the Reaction of NH_3 with Ga_2O_3/ZnO and $ZnGa_2O_4$: *In Situ* Time-Resolved XRD and XAFS Studies. *J. Phys. Chem. C* **2009**, *113*, 3650−3659.
(55) Moore, W. J.; Williams, E. L. Diffusion of Zinc and Oxygen in Zinc Oxide. *Discuss. Faraday Soc.* **1959**, *28*, 86−93.
(56) Nakagawa, T.; Sakaguchi, I.; Uematsu, M.; Sato, Y.; Ohashi, N.; Haneda, H.; Ikuhara, Y. Diffusion Model of Gallium in Single-Crystal ZnO Proposed from Analysis of Concentration-Dependent Profiles

DOI: 10.1021/acsnano.7b03891
ACS Nano 2017, 11, 8401−8412

Based on the Fermi-Level Effect. *Jpn. J. Appl. Phys.* **2007**, *46*, 4099−4101.
(57) Erhart, P.; Albe, K. Diffusion of Zinc Vacancies and Interstitials in Zinc Oxide. *Appl. Phys. Lett.* **2006**, *88*, 201918.
(58) Martin, M. Diffusion in Oxides. In *Diffusion in Condensed Matter: Method, Materials and Models*; Heitjeans, P., Kärger, J., Eds.; Springer: New York, 2005; pp 209−247.
(59) Huang, G.-Y.; Wang, C.-Y.; Wang, J.-T. Vacancy-Assisted Diffusion Mechanism of Group-III Elements in ZnO: an *Ab Initio* Study. *J. Appl. Phys.* **2009**, *105*, 073504.
(60) Steiauf, D.; Lyons, J. L.; Janotti, A.; Van de Walle, C. G. First-Principles Study of Vacancy-Assisted Impurity Diffusion in ZnO. *APL Mater.* **2014**, *2*, 096101.
(61) Sun, X.; Maeda, K.; Le Faucheur, M.; Teramura, K.; Domen, K. Preparation of $(Ga_{1-x}Zn_x)$ $(N_{1-x}O_x)$ Solid-Solution from $ZnGa_2O_4$ and ZnO as a Photo-Catalyst for Overall Water Splitting under Visible Light. *Appl. Catal., A* **2007**, *327*, 114−121.
(62) Zeitvogel, F.; Schmid, G.; Hao, L.; Ingino, P.; Obst, M. ScatterJ: An ImageJ Plugin for the Evaluation of Analytical Microscopy Datasets. *J. Microsc.* **2016**, *261*, 148−156.

DOI: 10.1021/acsnano.7b03891
ACS Nano 2017, 11, 8401−8412